MDPI

Cu-Doped SrTiO$_3$ Nanostructured Catalysts for CO$_2$ Conversion into Solar Fuels Using Localised Surface Plasmon Resonance

Lorenzo Rizzato [1,*], Jonathan Cavazzani [1], Andrea Osti [1], Marco Scavini [2] and Antonella Glisenti [1,*]

[1] Department of Chemical Sciences, University of Padova, Via F. Marzolo, 1, 35131 Padova, Italy; jonathan.cavazzani@phd.unipd.it (J.C.); andrea.osti.1@phd.unipd.it (A.O.)
[2] Department of Chemistry, University of Milano, Via Golgi, 19, 20133 Milano, Italy; marco.scavini@unimi.it
[*] Correspondence: lorenzo.rizzato.1@phd.unipd.it (L.R.); antonella.glisenti@unipd.it (A.G.)

Abstract: Carbon dioxide valorisation is one of the most discussed topics amongst researchers; indeed, finding a way to significantly reduce CO$_2$ concentration in the atmosphere is crucial in order to mitigate climate change effects in the next decades. In this study, SrTiO$_3$-supported Cu nanoparticles are exploited as Localised Surface Plasmon Resonance (LSPR)-mediated catalysts for CO$_2$ reduction. The materials were prepared via sol–gel citrate route methodology, inserting Cu as a dopant in the perovskite structure; reducing treatments at different temperatures were performed to promote copper atom exsolution, thus forming nanostructures upon the surface. The perovskitic structure was confirmed via ex situ and operando XRD analysis, while compositional analysis was carried out through XPS and EDS; SEM and TEM images revealed morphological changes with different reducing treatments, and bulk reducibility was analysed with H$_2$-TPR, revealing different Cu species in the material. Band gap analysis via DRS showed the successful incorporation of copper in the perovskite, affecting the light absorption properties. Finally, catalytic tests showed that copper nanoparticles play a role in CO$_2$ activation with sunlight, proving that LSPR could be exploited for catalytic means.

Keywords: photocatalysis; Sr$_{0.9}$TiO$_3$ perovskites; CO$_2$ valorisation; Cu doping

1. Introduction

As one of the most discussed topics in the last decade, carbon dioxide has gained much attention due to its high environmental impact, endangering ecosystems and human society survival. CO$_2$ emissions have been raising annually for more than 100 years [1], contributing 70% of the overall GHG (greenhouse gas) concentration [2] and accelerating global warming [3], thus increasing extreme climate events such as hurricanes, floods and droughts [4]. As an IR-active molecule [5], CO$_2$ can trap radiation from sunlight and Earth, contributing to the problem of global warming [6]. From the work of the Intergovernmental Panel on Climate Change (IPCC), it is estimated that about 730 additional trees should be grown to contain the anthropogenic CO$_2$ emissions of one single person [7]. For this reason, science is making a great effort to find alternative ways to convert carbon dioxide into useful and valuable chemical products; however, the unfavourable thermodynamics of CO$_2$ make the activation difficult to achieve in normal conditions [8]. Indeed, high C-O bond energy and high stability raise the activation energy required to adsorb molecules onto the catalysts surface and trigger bond cleavage [9].

To address the thermodynamic problem of CO$_2$ activation, different approaches have been explored from the early 1970s; different methodologies have been studied so far, including different energy vectors such as electricity, heat and photons [10–12]. Moreover, different classes of catalysts, including metal oxides, perovskites, metal–organic frameworks (MOFs), MXenes, metal complexes and many others [13–16], are currently

under investigation. From the large plethora of catalytic processes studied so far, the photocatalytic pathway has produced interesting results: using solar light as an energy vector greatly reduces the environmental impact of the process, as the energy source that drives the reaction is sustainable and readily available [17]. Moreover, alternative catalytic methods, such as thermocatalysis or electrocatalysis, often require high temperatures and pressures, thus resulting in harsher conditions and less sustainable processes.

The difficult C–O bond cleavage and the short charge lifetime before recombination in the catalyst inhibit the photoactivation of carbon dioxide, worsening the conversion rates at ambient temperature and pressure [17,18]. For these reasons, catalyst design is crucial in order to ensure that a high number of electrons are generated via visible light and effective e^-/h^+ separation. Achieving these characteristics would provide efficient CO_2 activation and reduction [19]; however, catalytic active sites with optimal carbon dioxide adsorption and desorption properties must be present on the catalyst surface. To overcome these challenges, catalyst design can exploit nanocomposites such as surface-decorated nanostructures; indeed, Localised Surface Plasmon Resonance (LSPR) can be employed, given nanostructuresstrong interaction with the supporting material. Metallic nanoparticles (NPs) possess enhanced light harvesting properties, better light absorption and better electron/hole pair formation [20]. Moreover, the presence of an intense electromagnetic field in the plasmonic nanoparticle surroundings drives electrons to migrate towards the surface of the material, thus increasing the number of possible active sites in the catalyst [21]. Hot electrons, generated through LSPR excitation and injected into the photocatalytic supporting material, also enhance its catalytic performance; indeed, their high kinetic energy can trigger the photo-reductive process of CO_2 when transferred to the conduction band (CB) of the semiconductor. Plasmonic nanoparticles also possess the interesting possibility to change their light absorption properties with size, shape, composition and support interaction variations, making them suitable candidates for CO_2 reduction catalysts [22,23]. Indeed, finding the best combination of physical properties that match the reaction requirements is crucial for achieving good performance and effectively converting carbon dioxide into useful chemical products.

A different class of materials may be employed in the photocatalytic activation of carbon dioxide. MOFs, as an example, are widely studied for their tuneable porous structures that could preferentially coordinate reactants towards favourable interaction [24], but they are difficult to synthesise. Several simple metal oxides have revealed promising activities towards the formation of various products, such as CO, CH_4 or methanol [25,26]. An interesting class of inorganic compounds is polycationic oxides, in particular perovskites; this class of catalysts is widely studied for different catalytic applications and possesses good tunability regarding numerous properties [27,28]. Indeed, compositional changes affect the material structural and electronic behaviour, thus making these mixed oxides interesting for a great number of applications, including photocatalysis [29]. In general, oxide-based simple perovskites are composed of an ABO_3 structure, with A and B being 12- and 6-coordinated cations, respectively; the correct selection of these cations allows them to develop active surface sites with respect to CO_2 reduction.

As one of the most studied materials for photocatalytic applications, $SrTiO_3$ could be a feasible choice for the photoreduction of CO_2, given its good stability in reducing atmospheres and in a wide range of temperatures [30]. However, its large band gap of 3.2 eV and its short charge lifetime makes it difficult to be used with visible light and for catalytic applications [31], as the catalyst–gas interaction process is relatively slow (>100 ps), while charge recombination occurs with shorter times (100 fs–100 ps) [32]; thus, optimisation of the material is crucial for slowing the recombination rate and shifting the absorption range towards a higher wavelength. Doping the B-site of the perovskite with an aliovalent cation results in band structure modification, introducing defect levels that narrow the band gap; additionally, defect centres can act as trap sites, extending charge lifetime [33,34]. Different kinds of metals can be taken into consideration for $SrTiO_3$ doping. As for its catalytic properties and enhanced electron conductivity, Cu doping seemed to

be a feasible choice for the scope of this work [35,36]. Moreover, the formation of small and dispersed nanoparticles can beeasily achieved: it is the so-called exsolution [37,38], i.e., the formation of socketed nanoparticles on the surface of the oxide upon a thermal treatment in a reducing atmosphere. The exploitation of such a phenomenon can lead to the creation of a nanocomposite system composed of a supporting $SrTiO_3$-based material and surface-dispersed Cu nanoparticles (NPs); while the semiconductor possesses a good interaction with CO_2 and H_2, NPs can harvest light efficiently and provide hot electrons to the active site. Indeed, unlike other deposition methods, e.g., wet impregnation, the exsolved NPs interact more strongly with the supporting material and are characterised by smaller dimensions, higher dispersion and enhanced stability. Thus, an increased number of active sites and better charge injection properties in the perovskite are expected.

In this work, a plasmonic-assisted photocatalytic approach to carbon dioxide activation, using an economic, scalable and low-energy-consumption reactor, is discussed. A perovskite-based semiconducting material, $Sr_{0.9}Ti_{0.95}Cu_{0.05}O_3$, was successfully synthetised using a sol–gel method, while surface decoration with small metallic nanoparticles was achieved through exsolution. The starting perovskite was chosen to be A-site-deficient to facilitate exsolution under a hydrogen atmosphere. Exsolution was studied as a function of the reduction temperature up to 700 °C; indeed, the exsolution environment deeply affects the type and surface distribution of copper NPs and thus the photocatalytic behaviour. The sample compositions and treatment temperatures are summarised in Table 1. The prepared Cu NP/titanate nanocomposite catalysts were characterised from structural, electronic and functional points of view and compared with the corresponding undoped material ($Sr_{0.9}TiO_3$), showing promising activity towards CO_2 reduction.

Table 1. Summary of specific surface area, grain size and pore size of STO and STCuO samples.

Sample	Composition	SSA (m^2/g)	Grain Size (nm) [1]	Mean Pore Size (nm) [2]
STO	$Sr_{0.9}TiO_3$	5.9	74.6	25.5
STCuO	$Sr_{0.9}Ti_{0.95}Cu_{0.05}O_3$	2.5	94.6	17.4
STCuO-r300	$Sr_{0.9}Ti_{0.95}Cu_{0.05}O_3$	-	100.9	-
STCuO-r500	$Sr_{0.9}Ti_{0.95}Cu_{0.05}O_3$	-	80.5	-
STCuO-r700	$Sr_{0.9}Ti_{0.95}Cu_{0.05}O_3$	-	67.9	-

[1] Calculated via Scherrer's equation using 40.0° reflection. [2] Calculated using BJH analysis.

2. Results and Discussion

2.1. Structural and Morphological Properties

From a structural investigation of $Sr_{0.9}TiO_3$ (STO) and $Sr_{0.9}Ti_{0.95}Cu_{0.05}O_3$ (STCuO) (Figure 1) performed using X-ray diffraction, the pattern of the as-prepared reference STO sample reveals the presence of cubic strontium titanate as the main phase (JCPDS no. 35-0734) [39] with little impurities of TiO_2 in anatase form (JCPDS no. 21-1272) [40]. Thus, the perovskitic structure is expected to be less A-site-deficient, as observed in other perovskitic structures [41]. Likewise, the STCuO sample shows a main phase, identified as cubic strontium titanate; as in STO, the STCuO sample shows reflections related to the presence of titanium dioxide impurities [42]. Other small reflections can be ascribed to the formation of mixed oxides phases, including copper-containing impurities, that suggest the incomplete incorporation of Cu in the perovskitic structure. From Rietveld refinements of the two as-prepared perovskites, a unit cell parameter of 3.9 Å could be calculated, consistent with the data found in the literature [43]. To optimise the exsolution process, operando XRD analysis was performed from RT to 800 °C in a vacuum to ensure low-oxygen partial pressure, thus ensuring the required driving force to promote oxygen vacancies (OVs) formation and metal atom diffusion. Rietveld analysis on the diffraction patterns obtained from STO and STCuO revealed different behaviour in the unit cell expansion, as can be seen in Figure 2. Indeed, the STO sample shows a linear expansion when the temperature is increased, as observed in the literature; conversely, Cu-doped strontium titanate does not follow the same expansion rate, showing two different linear

regions, one up to 400 °C and the other at higher temperatures. The first expansion process is slower in STCuO compared with STO, and it can be correlated with the partial exsolution of Cu from the oxide structure; indeed, the creation of a metal ion vacancy due to its diffusion causes unit cell shrinkage and a slowdown of its thermal expansion. At higher temperatures, the unit cell thermal expansion is not limited by the Cu diffusion, and the expansion rate becomes similar to the STO sample.
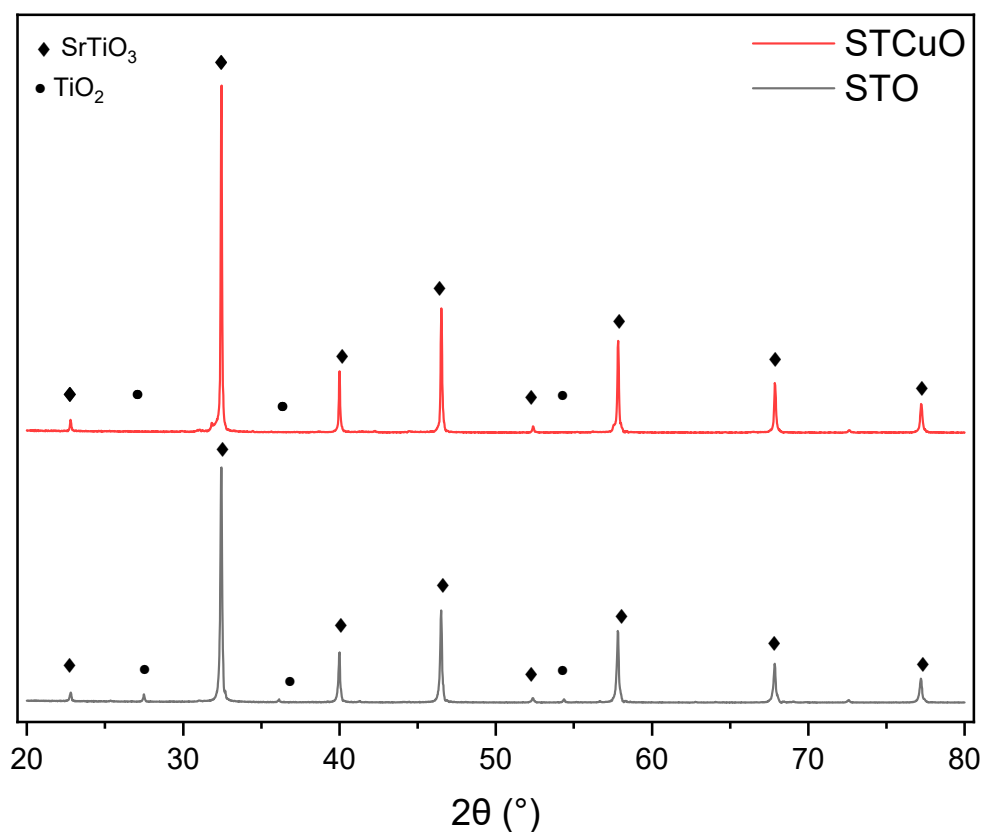

Figure 1. XRD patterns of STO and STCuO; the main perovskitic phase can be observed with squared dots, while the TiO_2 impurities are marked with circle dots.

Comparing the main peak positions of STCuO after the thermal treatment and reference STO [43], a slight shift towards lower angles can be observed; the aforementioned displacement can be related to a partial incorporation of Cu^{2+} ions into the perovskitic structure after the exsolution treatment, thus causing unit cell expansion as a consequence of the larger ionic radius of copper with respect to Ti^{4+} (Cu^{2+} = 0.73 Å > Ti^{4+} = 0.61 Å) [38].

Impurities due to mixed oxide reflections almost disappear after reduction (Figure 3). STCuO-r300 presents an XRD pattern similar to STCuO, confirming that the reduction treatment does not significantly affect the perovskitic structure. As found in the literature, a reducing atmosphere and adequate temperature trigger exsolution promote partial Cu diffusion from the first layers of the material and form Cu NPs on the surface [44]; however, exsolved metallic nanoparticles are generally small, making their detection hard in the XRD pattern. Samples STCuO-r500 and STCuO-r700 present a weak reflection at 43.5°, ascribed to metallic Cu. Atomic diffusion is a thermally activated phenomenon: simultaneously exsolved Cu cations can move more easily towards the surface. The reducing atmosphere allows the diffusion of elemental copper, while high temperatures promote particle aggregation; therefore, larger-dimension particles are expected at higher temperatures, significantly contributing to the diffraction pattern. When treating an STCuO sample at 700 °C, a new shift towards low angles can be observed (Figure S1), suggesting further expansion of the unit cell of the material; similar behaviour was described by Brennow et al. [45], who suggested the presence of Ti^{3+} ions after treating $SrTiO_3$ at a high temperature in reducing

atmospheres. Thus, the cell expansion can be related to the reduction of Ti^{4+} ions to Ti^{3+}, and to the subsequent incorporation of a certain amount of Cu^{2+} ions in the structure. Indeed, copper ion diffusion in the bulk could be enhanced by the lower ionic radius mismatch between Cu^{2+} and Ti^{3+} with respect to Ti^{4+}, thus promoting the formation of nanoparticles on the surface of the material.
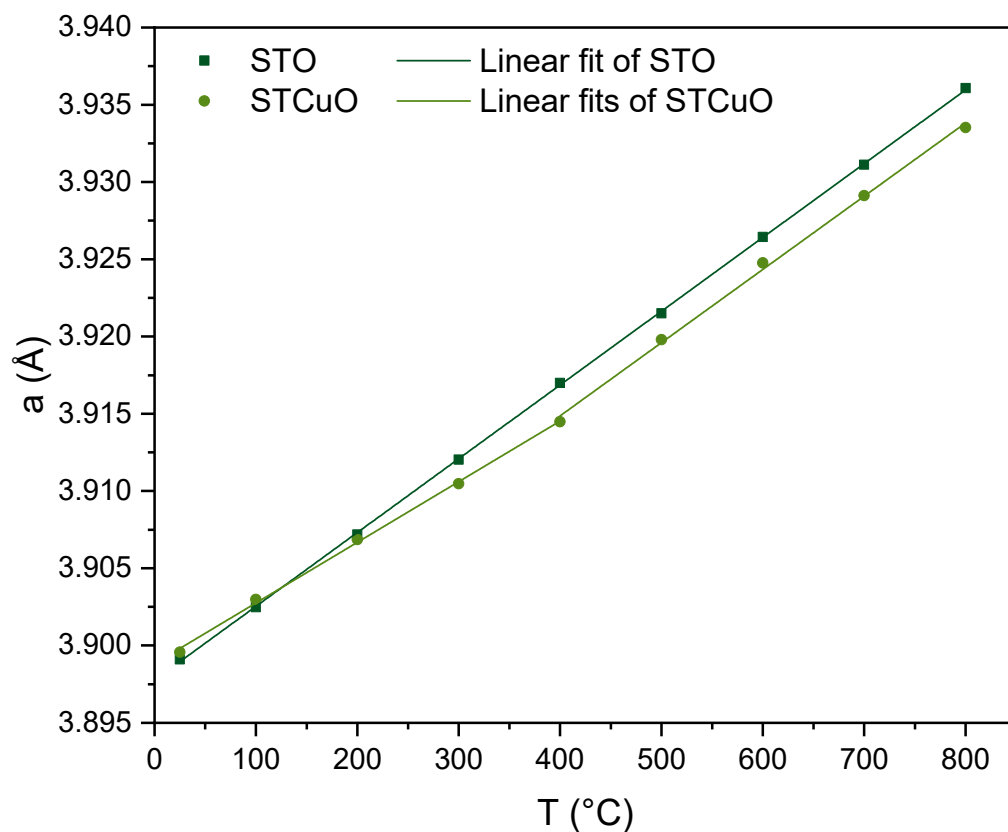

Figure 2. Cell parameter variation in STO and STCuO with temperature in low-oxygen partial pressure conditions. Linear cell expansion is observed for the undoped strontium titanate, while two regions can be distinguished, with two different expansion rates.
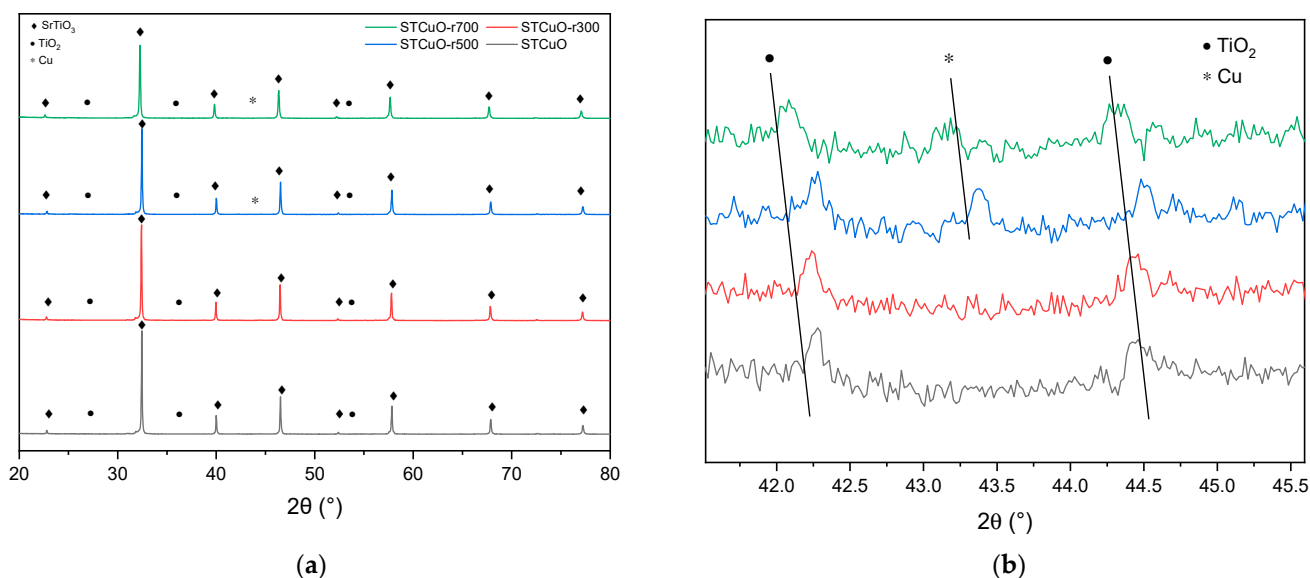

Figure 3. XRD pattern of as-prepared STCuO and of reduced STCuO at different temperatures (**a**); an enlargement in the metallic Cu region is presented (**b**).

From the BET analysis of N_2 adsorption–desorption isotherms, a type II isotherm together with an H3 hysteresis is observed for STO and for the Cu-doped counterpart (Figure S2); therefore, a macroporous material with little mesopores is expected from these observations. The specific surface area (SSA) of the strontium titanate is 5.9 $m^2 \cdot g^{-1}$, while the analysis of the doped perovskite results in a 2.5 $m^2 \cdot g^{-1}$ surface area, consistent with the literature data for a similar structure and synthetic procedure [46].

When comparing these results with the BJH pore distribution (Figure S3a,b), a higher density of mesopores, ranging from 2 to 20 $cm^3 \cdot g^{-1} \cdot nm^{-1}$, can be observed in the undoped sample with respect to STCuO; this evidence is consistent with the lower surface area and the more compact morphology revealed via SEM analysis in STCuO.

The atomic composition of the catalysts (Table 2) was determined using both energy-dispersive X-ray spectroscopy (EDS) and X-ray photoelectron spectroscopy (XPS) to gain information from different depths (with XPS being much more surface-sensitive). Therefore, compositional analysis and a comparison between sub-surface (EDS) and surface (XPS) measurements were performed, only considering metallic cations, as the EDS analysis on oxygen did not match the desired accuracy and reliability; the full XPS quantitative analyses are presented in Table S1. Composition-wise, the pure STO sample presents a slight excess of Sr in the first bulk and on the surface, probably also related to the formation of TiO_2 impurities during the synthetic process; comparing the EDS and the XPS compositions, a significant difference can be observed, consistent with the surface segregation of Sr. The presence of XPS peaks at 132.4 and 288.9 eV in the high-resolution spectra of the Sr 3d and C 1s regions, respectively, is symptomatic of Sr carbonate formation. In STCuO, the surface segregation of Sr is less evident, while the Ti content slightly changes between samples, generally showing a small deficiency with respect to the nominal composition.

Table 2. Elemental composition calculated from theoretical chemical formula; XPS and EDS data of STO, STCuO and STCuO reduced at different temperatures.

Element	Sample	Element Concentration		
		Nominal	EDS	XPS
Sr	STO	0.47	0.52	0.55
	STCuO	0.47	0.42	0.48
	STCuO-r300	0.47	0.41	0.47
	STCuO-r500	0.47	0.42	0.48
	STCuO-r700	0.47	0.47	0.47
Ti	STO	0.53	0.48	0.45
	STCuO	0.50	0.46	0.49
	STCuO-r300	0.50	0.46	0.49
	STCuO-r500	0.50	0.48	0.49
	STCuO-r700	0.50	0.46	0.50
Cu	STO	-	-	-
	STCuO	0.03	0.12	0.03
	STCuO-r300	0.03	0.13	0.04
	STCuO-r500	0.03	0.10	0.03
	STCuO-r700	0.03	0.07	0.03

Comparing sample composition between the as-prepared STCuO and the reduced samples, Cu content observed with EDS is higher with respect to the XPS signal; this could be related to the presence of Cu in the sub-surface of the catalyst. When reducing the doped perovskite, however, the EDS Cu content varies as a function of the reducing temperature: after the treatment at 300 °C, the Cu content is slightly increased, probably due to bulk Cu^{2+} ions that migrate towards the surface, a phenomenon already observed in perovskites [44], while at a higher temperature, the copper content decreases, approaching the nominal one. This behaviour could be ascribed as a new Cu incorporation process in the bulk due to the partial reduction of Ti^{4+}, as described above.

A comparison among the high-resolution XPS spectra of the various STCuO samples allows interesting insights; as mentioned before, the surface segregation of Sr is consistent with the formation of carbonate species on the surface. Besides the contribution due to carbonates ($3d_{5/2}$ around 132.4 eV), another doublet ($3d_{5/2}$ around 132.8 eV) can be ascribed to Sr–O bonding in the perovskite structure [47]. It is worth noting that no significant change in the peaks' position was found when comparing the fresh STCuO sample with the reduced materials, while a change in the carbonate/perovskite intensity ratio could be observed: increasing the reducing temperature, the carbonate-related signal decreased, thus showing that carbonates decompose and Sr is either embedded in the structure or can be converted to SrO.

As regards the Cu $2p_{3/2}$ region (Figure S6), the signal can be well fitted with multiple components; the main peak, at 934.5 eV for STCuO, is related to the presence of Cu^{2+} ions [48], while the second peak, at 943 eV, can be ascribed to the shake-up peak of Cu(II). When reducing the material, the position of the main component slightly changes, shifting to 935 eV in STCuO-r300 and then returning to its original position at 934.5 eV in STCuO-r700. No direct evidence of metallic Cu is present in the XPS spectra; however, the slight shift of the main peak observed in STCuO-r300 compared with STCuO can be ascribed to partial reduction of the Cu species [49,50].

Scanning electron microscopy images of STO (Figure 4) show a porous structure characterised by globular-shaped agglomerates with a high dimensional dispersion, ranging from 50 nm to 200 nm; fresh STCuO (Figure S4a) images indicate a similar morphology with a slightly more compact and less porous structure. Perovskite grains tend to merge after thermal treatment in a reducing atmosphere, reducing the porosity of the sample (Figure S4b–d).
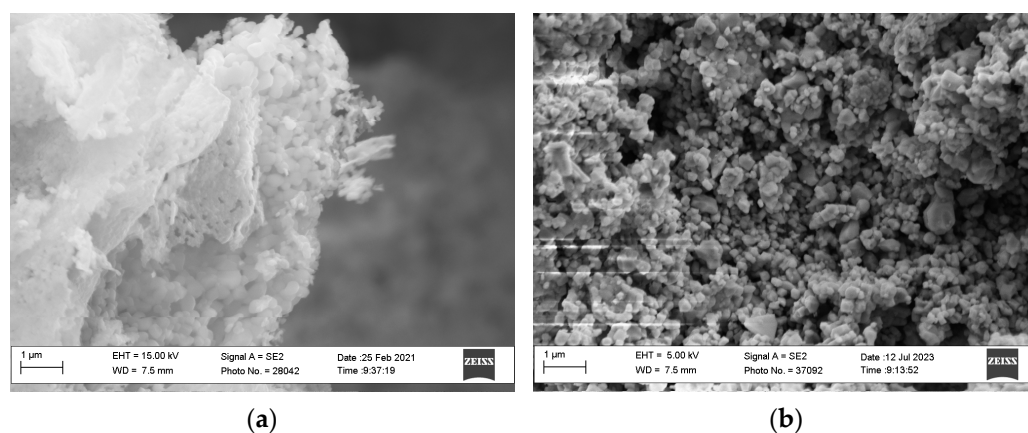

(**a**)   (**b**)

Figure 4. SEM images of STO (**a**) and STCuO (**b**). A different morphology can be observed: smaller grains appear on STO, while STCuO seems to possess a more compact structure.

To further confirm the presence of Cu nanostructures, TEM analysis was performed on the Cu-doped samples (Figure 5). The images revealed the same morphology, with dimensionally dispersed grains; on STCuO-r300, 3–5 nm particles were visible on the perovskitic agglomerates (Figure S5, circled). On the other samples, no visible signs of different nanostructures were clearly seen, therefore supporting the partial dissolution of the metallic structures at higher temperatures.

A two-step mechanism could explain the behaviour of STCuO: an initial exsolution step, occurring at low temperatures, involves Cu atoms in the bulk of the material diffusing towards the surface. In the second step, taking place at higher temperatures, the reducing atmosphere leads to the formation of Ti^{3+} ions and the subsequent diffusion of copper species towards the bulk. Moreover, the higher temperature reduction seems to enhance the growth of the nanoparticles, causing more dimensional dispersion and less stability of the system. As for the purpose of the study, the best reduction temperature was found to be

the lowest possible, as the Cu nanoparticle formation was enhanced and the agglomeration or diffusion to the bulk steps were limited.
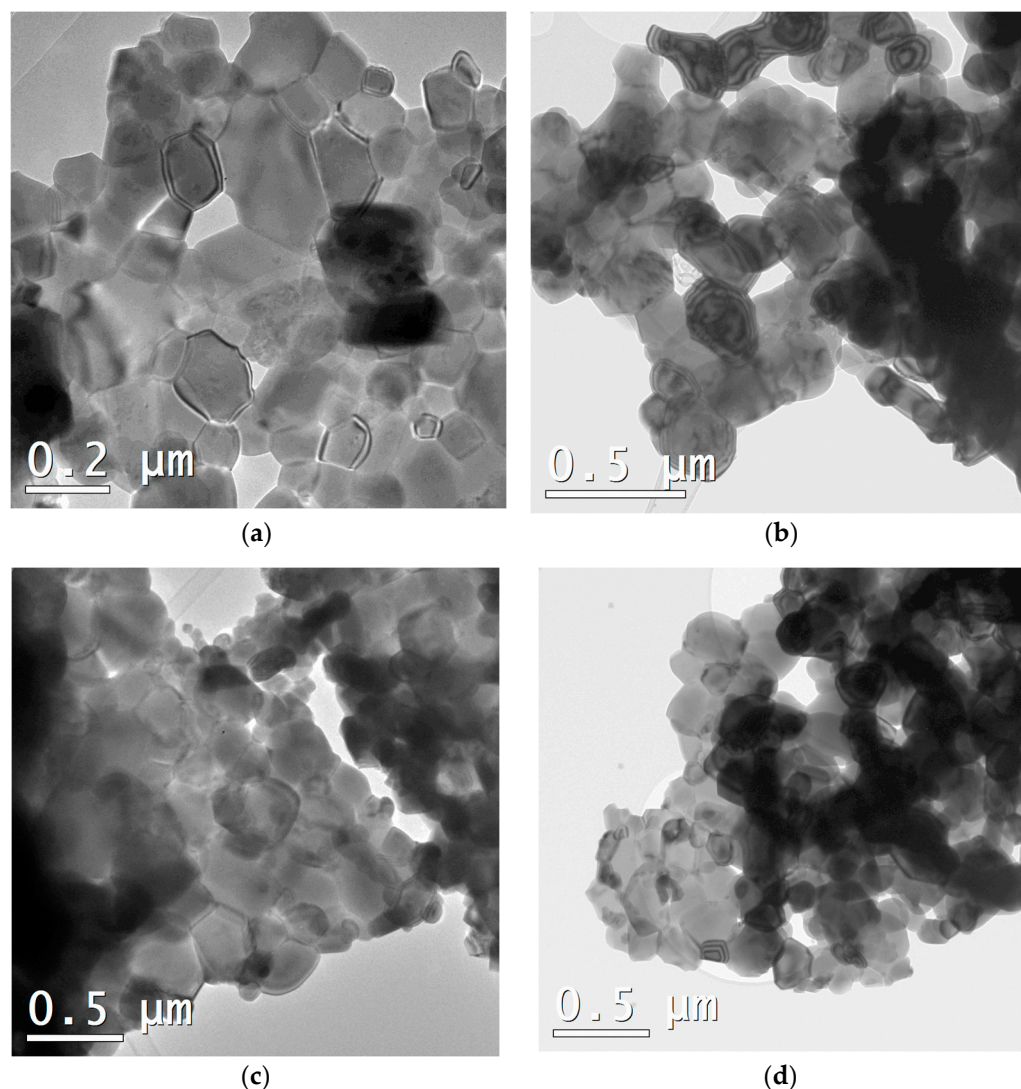

(a)

(b)

(c)

(d)

Figure 5. TEM images of as-prepared STCuO (**a**) and reduced samples: STCuO-r300 (**b**), STCuO-r500 (**c**) and STCuO-r700 (**d**).

2.2. Functional Properties

2.2.1. Bulk Reducibility

To gain information about the bulk reducibility of STO and STCuO, temperature-programmed reduction was performed (Figure 6). As-prepared strontium titanate TPR resulted in the absence of significant peaks, thus suggesting that no reductions occurred; however, Ti^{4+} to Ti^{3+} conversion was expected between 400 °C and 500 °C [51]. The absence of signals in this region could be ascribed to the small quantity of Ti species that were reduced in the process, which contributed to the signal for a fraction smaller than the instrument detection limit.

As regards STCuO, an intense signal could be observed at around 250 °C, which can be assigned to Cu^{2+} ions reduction; three contributions were derived from the peak fit, as can be seen in Figure S7. Different interpretations of this signal are found in the literature [52,53], assigning the components to different reduction processes: the subsequent $Cu^{2+} \rightarrow Cu^{+}$ and $Cu^{+} \rightarrow Cu^{0}$ reactions, or the presence of Cu ions with different chemical surroundings. Comparing the TPR signal with the XRD pattern, both interpretations are feasible. A two-step partial reduction of shallow copper together with various reduction

processes of Cu^{2+} species, present in grain boundaries, impurities and in the first layers, can occur, resulting in a reduction temperature shift to higher values with respect to pure CuO [54].
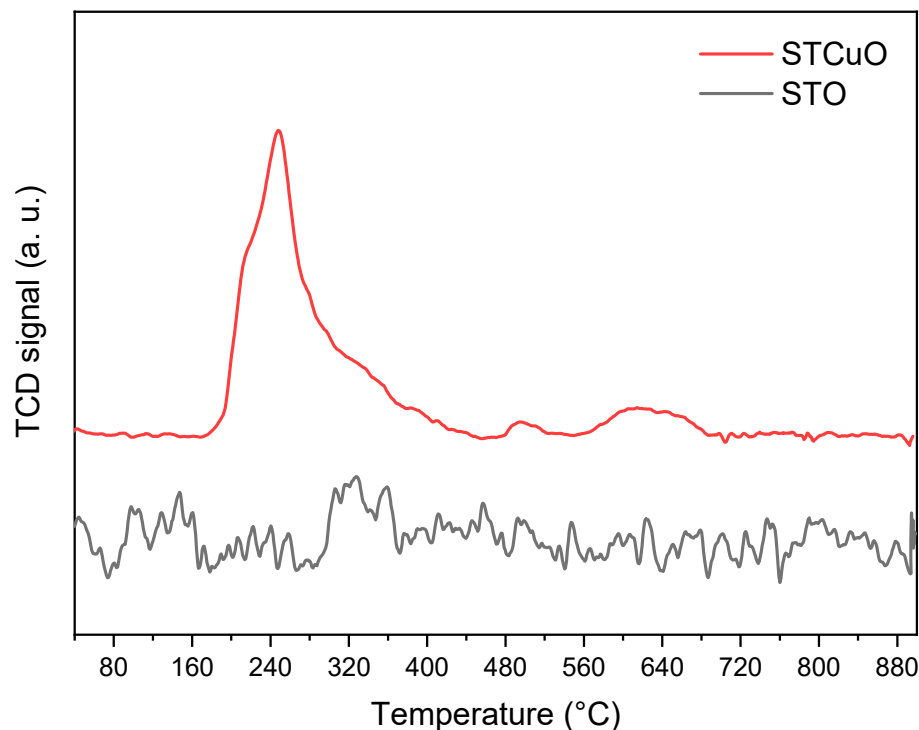

Figure 6. TPR signals of STO (black) and STCuO (red). No evident peaks were observed for undoped strontium titanate, while for STCuO, a set of low-temperature peaks, together with two higher temperature peaks, could be assigned to different reduction processes of Cu ions.

Two less intense signals are observed at around 500 °C and 620 °C; from the work of Gwóźdź et al. [54], these peaks could be ascribed to the reduction of Cu ions embedded in the material bulk, thus being more bound to the structure and therefore less reducible.

2.2.2. Electronic Properties

To further understand the properties of STCuO, diffuse reflectance UV-Vis spectra (DRS) were collected for STO and Cu-doped samples; subsequently, the Tauc plot was derived following Equations (2) and (3) described in Section 3.

From the Tauc plot (Figure 7) analysis, a band gap of 3.2 eV was found for the STO sample, which is in good agreement with the literature data. When doping the perovskite with Cu, the band gap decreases at 2.9 eV. From computational studies, a value of 2.2 eV [55] was expected; this suggests that the Cu atoms are only partially embedded in the perovskitic structure, thus further confirming the hypothesis previously made. The DRS spectra of reduced STCuO produce no significant changes in the band gap; this could be due to the extraction of Cu atoms from the sub-surface layers only, thus not significantly changing the perovskitic structure and Cu content in the bulk.

Comparing the two samples with respect to the minimum absorption wavelength, a redshift of 40 nm (from 385 nm to 425 nm) was found when inserting copper; this result indicates that better visible light absorption is expected from STCuO with respect to STO. The literature suggests that the insertion of copper into STO creates additional donor levels below the Fermi level, thus lowering the conduction band edge and narrowing the band gap [55]; this could be beneficial not only from a light absorption point of view, but also from a catalytic perspective: a higher energy valence band results in a better alignment with CO_2 reduction potentials [56]. To further confirm the position of the valence and the conduction band, studies are underway to investigate this more thoroughly.
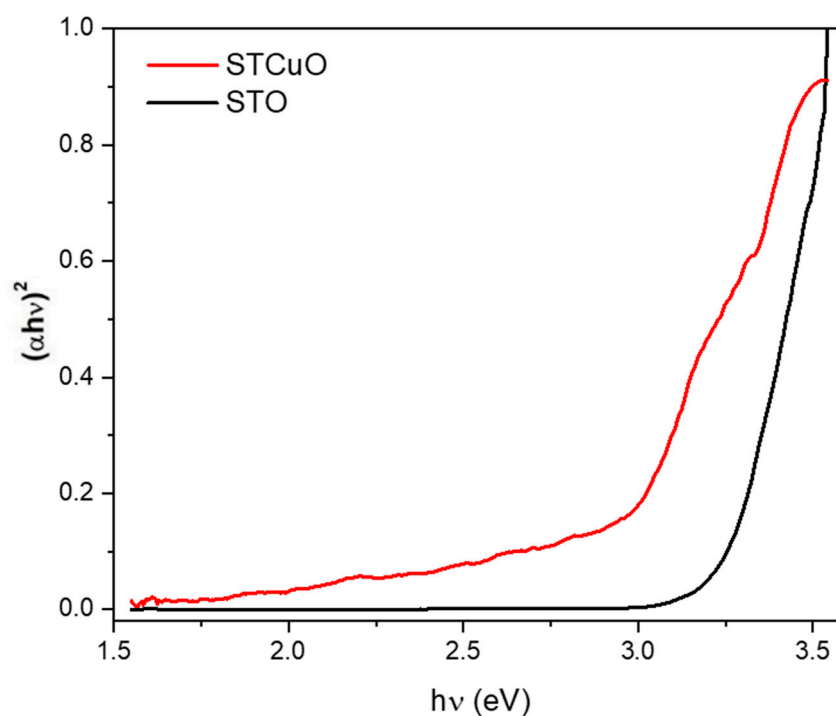
Figure 7. Tauc plot derived from DRS spectra of STO (black) and STCuO (red). A lower band gap can be calculated from the STCuO sample, thus confirming the Cu incorporation in the strontium titanate structure.

2.3. Catalytic Activity

Samples of STO and STCuO-r300 were tested for their ability to activate the CO_2 molecule with hydrogen in different conditions; a better understanding of which active sites are present in the materials and what type of interactions co-exist during the catalytic processes (Figure 8a) was expected. Additionally, the role of Cu nanoparticles was investigated to further evaluate the plasmonic resonance contribution to the reaction and confirm the results previously found [57].
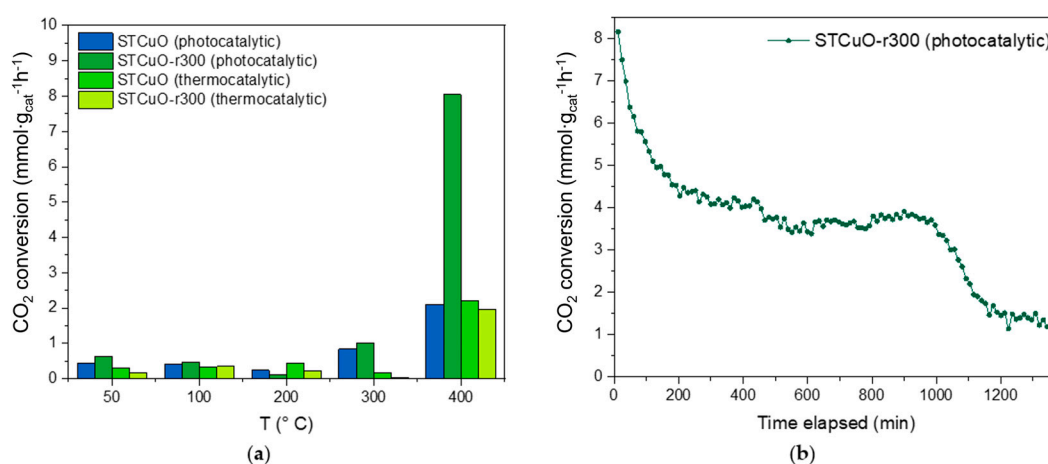

Figure 8. (**a**) Catalytic tests performed in dark and light conditions for STCuO and STCuO-r300 samples. Five temperatures (50, 100, 200, 300 and 400 °C) were chosen to analyse the behaviour of the materials in different thermodynamic conditions; (**b**) stability test conducted for 24 h in photo-assisted catalysis conditions with the STCuO-r300 sample.

The STO sample did not convert any significant amount of CO_2 during the reaction, either with only the thermal contribution or with the photo-assisted process. The absence

of activity in the presence of a light source was caused by the high band gap, which limited the light absorption to the UV part of the spectrum, and by the low number of active sites in which the CO_2 molecule could effectively adsorb.

When adding Cu in the material structure, the catalytic tests in dark conditions showed a significant CO_2 conversion of about 2 mmol$\cdot g_{cat}^{-1} \cdot h^{-1}$ at 400 °C; the conversion is ascribed to the presence of Cu sites that were able to activate the carbon dioxide molecule. Therefore, a significant contribution to the reaction is derived from the material structure and composition, meaning it is able to adsorb the reactant molecule and activate it during the reaction process. In the photo-assisted catalytic test, the presence of light further enhanced the onset shift, as 1 mmol$\cdot g_{cat}^{-1} \cdot h^{-1}$ CO_2 was converted at 300 °C. Indeed, the more efficient light absorption in the visible region leads to higher charge carrier production with respect to the thermocatalytic experiments, thus increasing the probability of reaction with the adsorbed CO_2 [58].

After reduction, the STCuO-r300 sample behaviour was similar to that of the fresh STCuO sample in light-off conditions: at 400 °C, the conversion difference was minimal, thus allowing us to conclude that Cu nanoparticles do not play a particular role in CO_2 reduction under dark conditions. However, when the material was exposed to visible light, the results differed significantly to the fresh STCuO: CO_2 conversion could already be observed at 50 °C; moreover, a four-times-higher conversion was determined at 400 °C compared to the fresh STCuO sample or to the same material not exposed to light. The conversion at 50 °C could be ascribed to the Cu nanoparticles on the surface that acted as active sites for CO_2 reduction and were photo-catalytically active. As the copper nanoparticle number was limited by the low doping content and the exsolution of the metal atoms embedded in the perovskitic structure was only partial, the number of active sites was consequently low, thus limiting the reaction rate. Moreover, the presence of Cu NPs can lead to the activation of their plasmonic behaviour, thus further enhancing catalytic activity; indeed, low temperatures favour the LSPR effect, limiting charge recombination and thus prolonging their lifetime, as well as enhancing the probability to reach surface active sites. By increasing temperature, catalytic activity in the presence of light decreases; this suggests the intervention of side-processes in the material, as phononic or electronic scattering, that prevent the LSPR from effectively activating the CO_2 molecule. As the temperature rises (300 °C), photo-assisted STCuO-mediated catalysis can still be observed; thus, a different catalytic mechanism can be hypothesised: at a higher temperature, the transport properties of STCuO change [59], allowing the generated SPR hot electrons to be injected more efficiently into the supporting material and therefore activating a larger number of active sites, enhancing the catalytic performance of the system.

As regards the products obtained from the catalytic tests, CO formation was observed for all of the active catalysts, as can be seen in Figure S8; however, the amount of carbon monoxide in the overall mixture was <5.3 mmol$\cdot g_{cat}^{-1} \cdot h^{-1}$, that is, the maximum sensibility of the instrument. Thus, the selectivity of the catalysts towards CO was found to be <66%. Comparing the CO TCD signals of STCuO and STCuO-r300, a similar trend to CO_2 conversion was observed: the catalysts in dark conditions exhibited reaction onset at about 320 °C, while the photo-assisted measurements indicated a lower onset at about 250 °C. Additionally, STCuO-r300 showed a 2-fold enhancement in CO production in photo-assisted conversion, confirming the hypothesis made above: light can significantly contribute to c performance, activating the catalytic sites and triggering CO_2-RR.

To address the stability of the STCuO material in working conditions, the catalyst was put under photo-assisted reaction conditions for 24 h; from the graph in Figure 8b, an initial significative decrease in the catalytic performance can be observed, followed by a plateau region and a second decrease between 17 h and 20 h after the start of the reaction. The evidence of two different deactivation regions can be ascribed to the presence of two different species of active sites, thus further confirming the hypothesis made above. From the literature, it seems that the inactivation of Cu active sites may occur due to partial oxidation of the metal [60], thus causing one of the conversion decrease curves [58]; the

other deactivation process could be related to the oxygen vacancies (OVs) that are filled during the process, as stated by Ma et al. [61]. Indeed, the presence of OVs in the supporting material is crucial for enhancing both catalytic and transport properties [62].

Comparing the performances of the catalysts with the state-of-the-art materials for CO_2 reduction, a significant difference can be spotted, showing lower performance of STCuO with respect to group VIII nanoparticles supported on Al_2O_3. Indeed, Ru, Rh and Ni nanostructures showed a much higher conversion rate, up to three orders of magnitude better than the present; indeed, a CO_2 reduction rate > 10 mol·g_{met}^{-1}·h^{-1} was observed in batch conditions for Ru-based materials. In spite of this, the STCuO-r300 catalyst showed better catalytic activity than conventional oxide-based perovskites, resulting in a 10-times-higher CO_2 conversion rate [63]. In addition, STCuO materials do not contain noble metals and are synthesised using only aqueous solutions, and the CO_2-RR is conducted using a cost-effective reactor; thus, the results obtained are interesting for the increased sustainability and scalability of the overall process.

To summarise, the presence of Cu nanoparticles on the surface of the perovskite results in better catalytic activity, due to the plasmonic effect that induces the excitation of hot electrons that either trigger a catalytic reaction on the nanoparticle surface or migrate to the supporting material active sites, as found in similar systems [64]. Copper atoms diffusion towards the surface can result in new defect points in the strontium titanate structure, thus making them possible active sites for effective CO_2 adsorption, making the catalyst performance better with respect to the undoped perovskite. Plasmonic effects can be visible at low temperatures (50 °C), in which charge carrier recombination is lower and the electron lifetimes are prolonged; additionally, a further contribution can be found at higher temperatures (400 °C), when the transport properties of strontium titanate allow effective hot electron injection through the active sites.

3. Materials and Methods

3.1. Synthetic Procedure

$Sr_{0.9}TiO_3$ (STO) was synthesised by means of a sol–gel/citrate route method, starting from $SrCO_3$ (98% Sigma-Aldrich, Hamburg, Germany) and $C_{12}H_{28}O_4Ti$ (97% Sigma-Aldrich, Gillingham, UK); the precursors were dissolved in an aqueous solution of nitric acid (≥65% Sigma-Aldrich, Schnelldorf, Germany) containing citric acid monohydrate as a complexing agent (≥99.0% Sigma-Aldrich, Vienna, Austria) in a citric acid/sum of metal cations equal to 1.9 and then neutralised with NH_3 (32%, Sigma-Aldrich, Darmstadt, Germany). The solution was aged at 80 °C for 24 h to form a wet gel; subsequently, the temperature was risen to 400 °C to ignite the self-combustion and therefore eliminate the organic framework and nitrates. $Sr_{0.9}Ti_{0.9}Cu_{0.05}O_3$ (STCuO) was synthesised using the same procedure, adding CuO (≥99% Sigma-Aldrich, St. Louis, MO, USA) as a precursor to the mother solution. The powders obtained from the combustion process were grinded and subsequently calcined at 1000 °C for 12 h with a temperature ramp of 6 °C/min.

The calcined samples containing Cu were treated in a 5% H_2/Ar atmosphere at different temperatures (300 °C, 500 °C and 700 °C) for 2 h with a temperature ramp of 6 °C/min, according to the observed TPR signal, to promote exsolution and gain information about the formation of nanoparticles and the structural and morphological changes in the sample.

3.2. Materials' Characterisation

XRD measurements were performed using a BRUKER D8 ADVANCE diffractometer with Bragg–Brentano geometry and using Cu K$_\alpha$ radiation (λ = 0.1548 nm). Data were collected with 2θ ranging from 20° to 80° and with a rate of 0.02 °/step and 0.35 s/step, while 40 kV and 40 mA were set as working conditions. Operando XRD analysis was performed by heating the samples from RT to 800 °C at 10 °C/min and collecting the diffraction pattern every 100 °C after equilibrating the system for 10 min; a constant oxygen partial pressure of p_{O2} = 10^{-7} atm was used in the chamber to ensure the driving force

needed to trigger exsolution. Scanning electron microscopy (SEM) images were taken using a 5 kV (for STCuO) and 15 kV (for STO) electron beam and secondary electron detection was conducted using a Zeiss Supra 40VP; energy-dispersive X-ray spectroscopy (EDX) was carried out at 20 kV using the same instrument. Specific surface area (SSA) evaluation was possible by means of N_2 physisorption isotherm analysis using a Micromeritics Asap 2020 Plus. The samples were loaded in a quartz reactor and degassed at 200 °C for 16 h; subsequently, N_2–sorption curves were obtained at liquid nitrogen temperature (T = 77 K) to evaluate the SSA from the BET equation. Temperature-programmed reduction (TPR) measurements were performed using the Micromeritics AutoChem II 2920 coupled with a TCD detector and a quartz tube reactor loaded with 50 mg of the sample. TPR measures were carried out by gassing the samples with 50 mL/min He and subsequently heating from RT to 900 °C at 10 °C/min in a 5% H_2/Ar atmosphere. XPS measurements were performed using a Thermo Scientific ESCALAB QXi. Extended spectra of the samples were acquired assuming the BE of the Au $4f_{7/2}$ to be 84.0 eV with respect to the Fermi level. Extended XPS spectra were acquired using a monochromatic Al source, with 100 eV pass energy and 0.5 eV/step, while detailed spectra were acquired with 20 eV pass energy and 0.1 eV/step. Surface compositions were determined after a Shirley-type background subtraction and using the Thermo Scientific sensitivity factors. Elemental composition analysis for EDS was performed considering the total metal concentration as the reference, as seen in Equation (1), where %M is the metal concentration and M^{sgn} is the signal of the same metal:

$$\%M = M^{sgn} / \sum M_i{}^{sgn} \tag{1}$$

To gain information about the electronic structure of the samples, Diffuse Reflectance Spectroscopy (DRS) was performed using an Oxford FT-1000 fluorimeter coupled with an integrating sphere. The spectra were acquired from 300 nm to 850 nm at 1 nm/step and 0.5 s/step. The collected data were then processed using the Tauc plot method to obtain the sample band gap; a direct allowed electronic transition was assumed based on the literature data [55], resulting in the following equation:

$$(KM \cdot h\nu)^{1/2} = A \cdot (h\nu - E_g) \tag{2}$$

where KM is the absorbance calculated using the Kubelka–Munk equation from the reflectance (R) spectra:

$$KM = (1 - R)^2 \cdot (2R)^{-1} \tag{3}$$

Catalytic tests were performed by loading 50 mg of the sample in a quartz tube reactor with a 6 mm internal diameter; the powder was compressed between two quartz wool flocks to ensure gas diffusion through the catalyst. Light-on/light-off tests were performed at different temperatures to evaluate the photo-thermocatalytic response of the materials. All photocatalytic tests were performed using an 85 W LED visible lamp with 200 mW/cm^2 power density measured using a Thorlabs S405C power meter coupled with a PM101 interface. A 100 mL/min stoichiometric gas mixture of 8% H2, 2% CO_2 and 90% Ar as a carrier gas was used for all of the tests; the reaction products were then analysed through gas chromatography, using an Agilent 7890 GC. To prevent water injection in the GC, the gas mixture was cooled with a chiller; for this reason, condensable products such as CH_3OH could not be detected. Thus, only the CO_2 conversion was quantified and not the products obtained from the reaction.

4. Conclusions

To summarise, $Sr_{0.9}TiO_3$ and $Sr_{0.9}Ti_{0.95}Cu_{0.05}O_3$ were successfully synthesised using a sol–gel citrate route, with minor impurities of TiO_2 for STO and spurious phase for STCuO. A cubic $SrTiO_3$ phase was observed for STO, while a distortion of the lattice was detected for STCuO, probably due to the insertion of copper in the structure. Thermal treatments at different temperatures in 5% H_2/Ar pointed out the general stability of the perovskitic phase in the reducing conditions, while evidence of copper nanoparticles was

spotted in STCuO-r300. The compositional analysis revealed a segregation of Cu in the fresh sample, which slightly increased at a low temperature and significantly decreased at higher reduction temperatures. Operando XRD analysis showed that the presence of Cu limits the cell thermal expansion below 400 °C, proving its diffusion outside of the perovskite cell. Copper insertion in the structure resulted in band gap narrowing and better visible light absorption; better valence band positioning was supposed, but more thorough studies have to be conducted to confirm this assumption. Comparing the catalytic performance of different samples, an increased CO_2 conversion rate of 8 mmol·g_{cat}^{-1}·h^{-1} was obtained with the reduced sample in photo-assisted conditions at 400 °C. A two-step reaction mechanism was proposed: firstly, plasmonic activation of the catalyst occurs, in which the Cu nanoparticles act as active sites and LSPR provides electrons for the reaction; secondly, LSPR-excited hot electrons are injected into the supporting material, activating the catalytic sites. To further understand the reaction process however, kinetics measurements are needed; specific in situ and operando techniques are crucial for observing the active sites evolution, the adsorption processes and the intermediates' formation, thus unravelling the reaction mechanism.

Supplementary Materials: The following supporting information can be downloaded at https://www.mdpi.com/article/10.3390/catal13101377/s1: Figure S1: XRD enlargement of Cu-doped samples; Figure S2: N_2 adsorption–desorption isotherms; Figure S3a: BJH adsorption curve; Figure S3b: BJH adsorption curve (enlargement); Figure S4a–d: SEM images of STCuO fresh and reduced samples; Figure S5: TEM enlargement of STCuO-r300; Figure S6: $Cu2p_{3/2}$ high-resolution XPS spectra for STCuO, STCuO-r300, STCuO-r500 and STCuO-r700; Figure S7: Peak fit of STCuO H_2-TPR; Figure S8: CO production curves; Table S1: XPS complete compositional analysis.

Author Contributions: Conceptualisation, L.R. and A.G.; methodology, L.R. and A.O.; validation, L.R., A.O. and J.C.; formal analysis, L.R., M.S., A.O. and J.C.; investigation, L.R., M.S., A.O. and J.C.; resources, A.G.; writing—original draft preparation, L.R.; writing—review and editing, A.O., J.C. and A.G.; visualisation, L.R., A.O. and J.C.; supervision, A.G.; project administration, L.R.; funding acquisition, A.G. All authors have read and agreed to the published version of the manuscript.

Data Availability Statement: All data are available upon request to the main author: lorenzo.rizzato.1@phd.unipd.it.

Conflicts of Interest: The authors declare no conflict of interest. The funders had no role in the design of the study; in the collection, analyses or interpretation of data; in the writing of the manuscript or in the decision to publish the results.

References

1. Etheridge, D.M.; Steele, L.P.; Langenfelds, R.L.; Francey, R.J.; Barnola, J.M.; Morgan, V.I. Natural and Anthropogenic Changes in Atmospheric CO_2 over the Last 1000 Years from Air in Antarctic Ice and Firn. *J. Geophys. Res. Atmos.* **1996**, *101*, 4115–4128. [CrossRef]
2. Yoro, K.O.; Daramola, M.O. CO_2 Emission Sources, Greenhouse Gases, and the Global Warming Effect. *Adv. Carbon Capture Methods Technol. Appl.* **2020**, 3–28. [CrossRef]
3. Cox, P.M.; Betts, R.A.; Jones, C.D.; Spall, S.A.; Totterdell, I.J. Acceleration of Global Warming Due to Carbon-Cycle Feedbacks in a Coupled Climate Model. *Nature* **2000**, *408*, 184–187. [CrossRef] [PubMed]
4. Perera, A.T.D.; Nik, V.M.; Chen, D.; Scartezzini, J.L.; Hong, T. Quantifying the Impacts of Climate Change and Extreme Climate Events on Energy Systems. *Nat. Energy* **2020**, *5*, 150–159. [CrossRef]
5. Taylor, J.H.; Benedict, W.S.; Strong, J. Infrared Spectra of H_2O and CO_2 at 500 °C. *J. Chem. Phys.* **1952**, *20*, 1884–1898. [CrossRef]
6. Anderson, T.R.; Hawkins, E.; Jones, P.D. CO_2, the Greenhouse Effect and Global Warming: From the Pioneering Work of Arrhenius and Callendar to Today's Earth System Models. *Endeavour* **2016**, *40*, 178–187. [CrossRef] [PubMed]

7.　Shukla, P.R.; Skea, J.; Calvo Buendia, E.; Masson-Delmotte, V.; Pörtner, H.-O.; Roberts, D.C.; Zhai, P.; Slade, R.; Connors, S.; van Diemen, R.; et al. *IPCC, 2019: Climate Change and Land: An IPCC Special Report on Climate Change, Desertification, Land Degradation, Sustainable Land Management, Food Security, and Greenhouse Gas Fluxes in Terrestrial Ecosystems*; Cambridge University Press: Cambridge, UK, 2019.

8.　Schneider, J.; Jia, H.; Muckerman, J.T.; Fujita, E. Thermodynamics and Kinetics of CO_2, CO, and H^+ Binding to the Metal Centre of CO_2 reductioncatalysts. *Chem. Soc. Rev.* **2012**, *41*, 2036–2051. [CrossRef]

9.　Zheng, Y.; Zhang, W.; Li, Y.; Chen, J.; Yu, B.; Wang, J.; Zhang, L.; Zhang, J. Energy Related CO_2 Conversion and Utilization: Advanced Materials/Nanomaterials, Reaction Mechanisms and Technologies. *Nano Energy* **2017**, *40*, 512–539. [CrossRef]

10.　Nahar, S.; Zain, M.F.M.; Kadhum, A.A.H.; Hasan, H.A.; Hasan, M.R. Advances in Photocatalytic CO_2 Reduction with Water: A Review. *Materials* **2017**, *10*, 629. [CrossRef]

11.　Resasco, J.; Bell, A.T. Electrocatalytic CO_2 Reduction to Fuels: Progress and Opportunities. *Trends Chem.* **2020**, *2*, 825–836. [CrossRef]

12.　Alam, M.I.; Cheula, R.; Moroni, G.; Nardi, L.; Maestri, M. Mechanistic and Multiscale Aspects of Thermo-Catalytic CO_2 Conversion to C 1 Products. *Catal. Sci. Technol.* **2021**, *11*, 6601–6629. [CrossRef]

13.　Li, X.; Xiong, J.; Tang, Z.; He, W.; Wang, Y.; Wang, X.; Zhao, Z.; Wei, Y. Recent Progress in Metal Oxide-Based Photocatalysts for CO_2 Reduction to Solar Fuels: A Review. *Molecules* **2023**, *28*, 1653. [CrossRef] [PubMed]

14.　Li, D.; Kassymova, M.; Cai, X.; Zang, S.Q.; Jiang, H.L. Photocatalytic CO_2 Reduction over Metal-Organic Framework-Based Materials. *Coord. Chem. Rev.* **2020**, *412*, 213262. [CrossRef]

15.　Zeng, S.; Kar, P.; Thakur, U.K.; Shankar, K. A Review on Photocatalytic CO_2 Reduction Using Perovskite Oxide Nanomaterials. *Nanotechnology* **2018**, *29*, 052001. [CrossRef] [PubMed]

16.　Nguyen, T.P.; Tuan Nguyen, D.M.; Tran, D.L.; Le, H.K.; Vo, D.V.N.; Lam, S.S.; Varma, R.S.; Shokouhimehr, M.; Nguyen, C.C.; Le, Q. Van MXenes: Applications in Electrocatalytic, Photocatalytic Hydrogen Evolution Reaction and CO_2 Reduction. *Mol. Catal.* **2020**, *486*, 110850. [CrossRef]

17.　Qian, R.; Zong, H.; Schneider, J.; Zhou, G.; Zhao, T.; Li, Y.; Yang, J.; Bahnemann, D.W.; Pan, J.H. Charge Carrier Trapping, Recombination and Transfer during TiO_2 Photocatalysis: An Overview. *Catal. Today* **2019**, *335*, 78–90. [CrossRef]

18.　Vu, N.-N.; Kaliaguine, S.; Do, T.-O.; Vu, N.; Kaliaguine, S.; Do, T. Critical Aspects and Recent Advances in Structural Engineering of Photocatalysts for Sunlight-Driven Photocatalytic Reduction of CO_2 into Fuels. *Adv. Funct. Mater.* **2019**, *29*, 1901825. [CrossRef]

19.　Neaţu, Ş.; Maciá-Agulló, J.A.; Garcia, H. Solar Light Photocatalytic CO_2 Reduction: General Considerations and Selected Bench-Mark Photocatalysts. *Int. J. Mol. Sci.* **2014**, *15*, 5246–5262. [CrossRef] [PubMed]

20.　Hou, W.; Cronin, S.B. A Review of Surface Plasmon Resonance-Enhanced Photocatalysis. *Adv. Funct. Mater.* **2013**, *23*, 1612–1619. [CrossRef]

21.　Hutter, E.; Fendler, J.H. Exploitation of Localized Surface Plasmon Resonance. *Adv. Mater.* **2004**, *16*, 1685–1706. [CrossRef]

22.　Chen, K.; Leong, E.S.P.; Rukavina, M.; Nagao, T.; Liu, Y.J.; Zheng, Y. Active Molecular Plasmonics: Tuning Surface Plasmon Resonances by Exploiting Molecular Dimensions. *Nanophotonics* **2015**, *4*, 186–197. [CrossRef]

23.　Xu, G.; Tazawa, M.; Jin, P.; Nakao, S.; Yoshimura, K. Wavelength Tuning of Surface Plasmon Resonance Using Dielectric Layers on Silver Island Films. *Appl. Phys. Lett.* **2003**, *82*, 3811–3813. [CrossRef]

24.　Klein, N.; Senkovska, I.; Gedrich, K.; Stoeck, U.; Henschel, A.; Mueller, U.; Kaskel, S. A Mesoporous Metal-Organic Framework. *Angew. Chem. Int. Ed.* **2009**, *48*, 9954–9957. [CrossRef] [PubMed]

25.　Kohno, Y.; Tanaka, T.; Funabiki, T.; Yoshida, S. Photoreduction of CO_2 with H_2 over ZrO_2. A Study on Interaction of Hydrogen with Photoexcited CO_2. *Phys. Chem. Chem. Phys.* **2000**, *2*, 2635–2639. [CrossRef]

26.　Inoue, T.; Fujishima, A.; Konishi, S.; Honda, K. Photoelectrocatalytic Reduction of Carbon Dioxide in Aqueous Suspensions of Semiconductor Powders. *Nature* **1979**, *277*, 637–638. [CrossRef]

27.　Zhang, G.; Liu, G.; Wang, L.; Irvine, J.T.S. Inorganic Perovskite Photocatalysts for Solar Energy Utilization. *Chem. Soc. Rev.* **2016**, *45*, 5951–5984. [CrossRef]

28.　Schanze, K.S.; Kamat, P.V.; Yang, P.; Bisquert, J. Progress in Perovskite Photocatalysis. *ACS Energy Lett.* **2020**, *5*, 2602–2604. [CrossRef]

29.　Tanaka, H.; Misono, M. Advances in Designing Perovskite Catalysts. *Curr. Opin. Solid State Mater. Sci.* **2001**, *5*, 381–387. [CrossRef]

30.　Luo, C.; Zhao, J.; Li, Y.; Zhao, W.; Zeng, Y.; Wang, C. Photocatalytic CO_2 Reduction over $SrTiO_3$: Correlation between Surface Structure and Activity. *Appl. Surf. Sci.* **2018**, *447*, 627–635. [CrossRef]

31.　Cheng, C.; Long, R. Charge-Compensated Doping Extends Carrier Lifetimes in $SrTiO_3$ by Passivating Oxygen Vacancy Defects. *J. Phys. Chem. Lett.* **2021**, *12*, 12040–12047. [CrossRef]

32.　Ghoussoub, M.; Xia, M.; Duchesne, P.N.; Segal, D.; Ozin, G. Principles of Photothermal Gas-Phase Heterogeneous CO_2 Catalysis. *Energy Env. Sci* **2019**, *12*, 1122–1142. [CrossRef]

33.　Konta, R.; Ishii, T.; Kato, H.; Kudo, A. Photocatalytic Activities of Noble Metal Ion Doped $SrTiO_3$ under Visible Light Irradiation. *J. Phys. Chem. B* **2004**, *108*, 8992–8995. [CrossRef]

34.　Xu, Y.; Liang, Y.; He, Q.; Xu, R.; Chen, D.; Xu, X.; Hu, H. Review of Doping $SrTiO_3$ for Photocatalytic Applications. *Bull. Mater. Sci.* **2022**, *46*, 6. [CrossRef]

35.　Rahman, Q.I.; Ahmad, M.; Misra, S.K.; Lohani, M. Efficient Degradation of Methylene Blue Dye over Highly Reactive Cu Doped Strontium Titanate ($SrTiO_3$) Nanoparticles Photocatalyst under Visible Light. *J. Nanosci. Nanotechnol.* **2012**, *12*, 7181–7186. [CrossRef]

36. Gawande, M.B.; Goswami, A.; Felpin, F.X.; Asefa, T.; Huang, X.; Silva, R.; Zou, X.; Zboril, R.; Varma, R.S. Cu and Cu-Based Nanoparticles: Synthesis and Applications in Catalysis. *Chem. Rev.* **2016**, *116*, 3722–3811. [CrossRef]

37. Neagu, D.; Tsekouras, G.; Miller, D.N.; Ménard, H.; Irvine, J.T.S. In Situ Growth of Nanoparticles through Control of Non-Stoichiometry. *Nat. Chem.* **2013**, *5*, 916–923. [CrossRef]

38. Cavazzani, J.; Squizzato, E.; Brusamarello, E.; Glisenti, A. Exsolution in Ni-Doped Lanthanum Strontium Titanate: A Perovskite-Based Material for Anode Application in Ammonia-Fed Solid Oxide Fuel Cell. *Int. J. Hydrogen Energy* **2022**, *47*, 13921–13932. [CrossRef]

39. Yeshodamma, S.; Hareesh, K.; Nagabhushana, H.; Dwivedi, J.; Petwal, V.C.; Sunitha, D.V. Influence of Electron Beam Irradiation on Structural, Thermo and Photoluminescence Properties of $SrTiO_3$:Sm^{3+} Nanophosphor. *Optik* **2020**, *223*, 165483. [CrossRef]

40. Mohamed, I.M.A.; Dao, V.D.; Yasin, A.S.; Mousa, H.M.; Mohamed, H.O.; Choi, H.S.; Hassan, M.K.; Barakat, N.A.M. Nitrogen-Doped&SnO_2-Incoportaed TiO_2 Nanofibers as Novel and Effective Photoanode for Enhanced Efficiency Dye-Sensitized Solar Cells. *Chem. Eng. J.* **2016**, *304*, 48–60. [CrossRef]

41. Osti, A.; Rizzato, L.; Cavazzani, J.; Glisenti, A. Optimizing Citrate Combustion Synthesis of A-Site-Deficient La,Mn-Based Perovskites: Application for Catalytic CH_4 Combustion in Stoichiometric Conditions. *Catalysts* **2023**, *13*, 1177. [CrossRef]

42. Zhang, J.Y.; Boyd, I.W.; O'Sullivan, B.J.; Hurley, P.K.; Kelly, P.V.; Sénateur, J.P. Nanocrystalline TiO_2 Films Studied by Optical, XRD and FTIR Spectroscopy. *J. Non-Cryst. Solids* **2002**, *303*, 134–138. [CrossRef]

43. Wu, C.; Li, J.; Fan, Y.; Xing, J.; Gu, H.; Zhou, Z.; Lu, X.; Zhang, Q.; Wang, L.; Jiang, W. The Effect of Reduced Graphene Oxide on Microstructure and Thermoelectric Properties of Nb-Doped A-Site-Deficient $SrTiO_3$ Ceramics. *J. Alloy. Compd.* **2019**, *786*, 884–893. [CrossRef]

44. Zhang, Z.; Chen, R.; Wang, L.; Chen, X.; Ding, J.; Zhang, J.; Wan, H.; Guan, G. Synergistic Effect of Cu^{2+} and Cu^+ in $SrTiO_3$ Nanofibers Promotes the Photocatalytic Reduction of CO_2 to Methanol. *Appl. Surf. Sci.* **2023**, *609*, 155297. [CrossRef]

45. Blennow, P.; Hagen, A.; Hansen, K.K.; Wallenberg, L.R.; Mogensen, M. Defect and Electrical Transport Properties of Nb-Doped $SrTiO_3$. *Solid State Ion.* **2008**, *179*, 2047–2058. [CrossRef]

46. Zhang, W.; Du, L.; Bi, F.; He, H. A Novel $SrTiO_3$/HZSM-5 Photocatalyst Prepared by Sol–Gel Method. *Mater. Lett.* **2015**, *157*, 103–105. [CrossRef]

47. Divya, A.; Mathavan, T.; Harish, S.; Archana, J.; Benial, A.M.F.; Hayakawa, Y.; Navaneethan, M. Synthesis and Characterization of Branchlet-like $SrCO_3$ Nanorods Using Triethylamine as a Capping Agent by Wet Chemical Method. *Appl. Surf. Sci.* **2019**, *487*, 1271–1278. [CrossRef]

48. Li, B.; Hong, J.; Ai, Y.; Hu, Y.; Shen, Z.; Li, S.; Zou, Y.; Zhang, S.; Wang, X.; Zhao, G.; et al. Visible-near-Infrared-Light-Driven Selective Oxidation of Alcohols over Nanostructured Cu Doped $SrTiO_3$ in Water under Mild Condition. *J. Catal.* **2021**, *399*, 142–149. [CrossRef]

49. Ghodselahi, T.; Vesaghi, M.A.; Shafiekhani, A.; Baghizadeh, A.; Lameii, M. XPS Study of the $Cu@Cu_2O$ Core-Shell Nanoparticles. *Appl. Surf. Sci.* **2008**, *255*, 2730–2734. [CrossRef]

50. Gaudin, P.; Fioux, P.; Dorge, S.; Nouali, H.; Vierling, M.; Fiani, E.; Molière, M.; Brilhac, J.F.; Patarin, J. Formation and Role of Cu^+ Species on Highly Dispersed CuO/SBA-15 Mesoporous Materials for SO_x Removal: An XPS Study. *Fuel Process. Technol.* **2016**, *153*, 129–136. [CrossRef]

51. Bai, L.; Polo-Garzon, F.; Bao, Z.; Luo, S.; Moskowitz, B.M.; Tian, H.; Wu, Z. Impact of Surface Composition of $SrTiO_3$ Catalysts for Oxidative Coupling of Methane. *ChemCatChem* **2019**, *11*, 2107–2117. [CrossRef]

52. López-Suárez, F.E.; Parres-Esclapez, S.; Bueno-López, A.; Illán-Gómez, M.J.; Ura, B.; Trawczynski, J. Role of Surface and Lattice Copper Species in Copper-Containing (Mg/Sr)TiO_3 Perovskite Catalysts for Soot Combustion. *Appl. Catal. B* **2009**, *93*, 82–89. [CrossRef]

53. Rodriguez, J.A.; Kim, J.Y.; Hanson, J.C.; Pérez, M.; Frenkel, A.I. Reduction of CuO in H_2: In Situ Time-Resolved XRD Studies. *Catal. Lett.* **2003**, *85*, 247–254. [CrossRef]

54. Gwóźdź, P.; Łącz, A.; Mizera, A.; Drożdż, E. Some Aspects of Cu Incorporation into $SrTiO_3$ Structure. *J. Therm. Anal. Calorim.* **2022**, *147*, 9949–9958. [CrossRef]

55. Rizwan, M.; Ali, A.; Usman, Z.; Khalid, N.R.; Jin, H.B.; Cao, C.B. Structural, Electronic and Optical Properties of Copper-Doped $SrTiO_3$ Perovskite: A DFT Study. *Phys. B Condens. Matter* **2019**, *552*, 52–57. [CrossRef]

56. Huang, H.; Song, H.; Kou, J.; Lu, C.; Ye, J. Atomic-Level Insights into Surface Engineering of Semiconductors for Photocatalytic CO_2 Reduction. *J. Energy Chem.* **2022**, *67*, 309–341. [CrossRef]

57. Huang, H.B.; Yu, K.; Zhang, N.; Xu, J.Y.; Yu, X.T.; Liu, H.X.; Cao, H.L.; Lü, J.; Cao, R. Localized Surface Plasmon Resonance Enhanced Visible-Light-Driven CO_2 Photoreduction in Cu Nanoparticle Loaded ZnInS Solid Solutions. *Nanoscale* **2020**, *12*, 15169–15174. [CrossRef]

58. Li, Z.; Zhu, G.; Zhang, W.; Zhu, L.; Cao, B.; Gao, J.; Shi, X.; Huang, Y.; Liu, P.; Hojamberdiev, M. Dual-Functional Copper (Cu0/Cu2+)-Modified SrTiO3-δ Nanosheets with Enhanced Photothermal Catalytic Performance for CO_2 Reduction and H_2 Evolution. *Chem. Eng. J.* **2023**, *452*, 139378. [CrossRef]

59. Shang, D.S.; Sun, J.R.; Shi, L.; Wang, J.; Wang, Z.H.; Shen, B.G. Electronic Transport and Colossal Electroresistance in $SrTiO_3$:Nb-Based Schottky Junctions. *Appl. Phys. Lett.* **2009**, *94*, 052105. [CrossRef]

60. Kang, Q.; Wang, T.; Li, P.; Liu, L.; Chang, K.; Li, M.; Ye, J. Photocatalytic Reduction of Carbon Dioxide by Hydrous Hydrazine over Au–Cu Alloy Nanoparticles Supported on $SrTiO_3$/TiO_2 Coaxial Nanotube Arrays. *Angew. Chem.* **2015**, *127*, 855–859. [CrossRef]

61. Ma, H.; Yang, W.; Tang, H.; Pan, Y.; Li, W.; Fang, R.; Shen, Y.; Dong, F. Enhance the Stability of Oxygen Vacancies in SrTiO$_3$ via Metallic Ag Modification for Efficient and Durable Photocatalytic NO Abatement. *J. Hazard. Mater.* **2023**, *452*, 131269. [CrossRef]
62. Rusevich, L.L.; Tyunina, M.; Kotomin, E.A.; Nepomniashchaia, N.; Dejneka, A. The Electronic Properties of SrTiO$_3$-δ with Oxygen Vacancies or Substitutions. *Sci. Rep.* **2021**, *11*, 23341. [CrossRef] [PubMed]
63. Teh, Y.W.; Chee, M.K.T.; Kong, X.Y.; Yong, S.T.; Chai, S.P. An Insight into Perovskite-Based Photocatalysts for Artificial Photosynthesis. *Sustain. Energy Fuels* **2020**, *4*, 973–984. [CrossRef]
64. Luo, S.; Ren, X.; Lin, H.; Song, H.; Ye, J. Plasmonic Photothermal Catalysis for Solar-to-Fuel Conversion: Current Status and Prospects. *Chem. Sci.* **2021**, *12*, 5701–5719. [CrossRef] [PubMed]